On the Growth, Structure and Dynamics of P3EHT Crystals

On the Growth, Structure and Dynamics of P3EHT Crystals

Gregório C. Faria[†1*], Duc T. Duong[†,2], Giovanni Paro da Cunha[1], Philipp Selter[3], Lasse Arnt Strassø[4], Emily C. Davidson[5], Rachel A. Segalman [5,6], Michael Ryan Hansen[3], Eduardo Ribeiro deAzevedo[1*], Alberto Salleo[2]

[1] *Instituto de Física de São Carlos, Universidade de São Paulo, CP 369, 13660-970, São Carlos, SP, Brazil*

[2] *Department of Materials Science and Engineering, Stanford University, Stanford, California 94305, USA*

[3] *Institute of Physical Chemistry, Westfälische Wilhelms-Universität Münster, Corrensstr. 28/30, D-48149 Münster, Germany*

[4] *Interdisciplinary Nanoscience Center, Aarhus University, Gustav Wieds Vej 14, DK-8000 Aarhus C, Denmark*

[5] *Departments of Chemical Engineering, University of California, Santa Barbara, Santa Barbara, California 93106, United States*

[6] *Departments of Materials, University of California, Santa Barbara, Santa Barbara, California 93106, United States*

[†]G. C. Faria and D.T. Duong contributed equally to this work.

ABSTRACT:

We employ X-Ray diffraction, NMR and UV-vis spectroscopy techniques to shed light on the structure, molecular mobility and crystallization of a prototypical semiconducting polymer poly(3-(2'ethylhexyl)thiophene) (P3EHT). Grazing-incidence X-ray diffraction (GIXD) and high-field ^{1}H-^{1}H double-quantum NMR reveal a tilt of the thiophene rings along the main chains, while high resolution ^{13}C solid-state NMR methods show the presence of highly mobile side-chains. Taken together, the data reveal a high amount of free volume between adjacent chains in the crystalline phase, most likely owing to the additional steric hindrance from the branched ethyl group of the hexyl side chains. Additionally, the aforementioned methods allow us to confirm that crystallization in P3EHT occurs in a one-dimensional fashion along the polymer backbone. An extended model based on the Avrami principles is used to fit the experimental results to extract key parameters, such as nucleation rate and density, that govern these crystallization processes. The results show significantly reduced rates of crystallization in thin P3EHT thin films due to polymer chain confinement effects.

KEYWORDS: Conjugated polymers, microstructure, molecular mobility, polymer crystallization, extended Avrami model

1. INTRODUCTION

Semiconducting polymers have attracted significant attention over the last several decades owing to their solution processability, chemical tunability and continually improving electrical properties. To date, experimentally obtained hole mobilities of conjugated polymers have surpassed the mark of 1 cm^2 V^{-1} s^{-1}, several orders of magnitude higher than when they were first discovered in the 1980s[1–3]. These materials have been successfully used for applications in flexible transistors[4], sensors[5,6], displays and lighting[7–9], photovoltaics[10,11]and neural stimulations[12,13], to name a few.

Regardless of device architectures and material requirements specific to the application, efficient transport of electrons and holes through a semicrystalline polymer network is essential for optimal electrical function. Enhanced charge transport leads to higher power gain in organic field effect transistors (OFETs)[14,15], higher luminance in organic light-emitting diodes (OLEDs)[16,17] and higher power conversion efficiencies in organic photovoltaics (OPVs)[10,11,18]. While substrate effects[19,20] and processing conditions[20–22] can all have significant impacts on these performance parameters, the intrinsic ability of a particular material to transport charge sets an upper boundary and depends on its solid-state microstructure and molecular packing.

An important bottleneck for charge transport is interchain charge hopping via overlapping π-π molecular orbitals. Unsurprisingly this process is strongly dependent on the crystal structure of the particular polymer, which dictates the orbital overlap. Because semiconducting polymers are weakly diffracting and there are very few cases where conjugated polymer single crystals have been grown[23–27], the exact molecular packing and crystal properties are not known for most materials. From a materials perspective, we are interested in the interchain packing motif, the conformation and dynamics of the solubilizing side chains, and the processes that govern the formation of the crystalline structure. Together these insights provide a thorough and complete picture of atomic positions and dynamics within a polymer crystal.

In this work, we present a detailed study of the growth, structure and dynamics of crystals for a model polythiophene polymer, namely poly(3-(2'-ethyl)hexylthiophene) (P3EHT). Like most conjugated polymers, P3EHT exhibits semicrystalline solid-state morphologies with ordered domains distributed among otherwise amorphous, disordered regions. Due to its low melting point, P3EHT further exhibits significantly slower crystallization kinetics at low temperatures allowing for detailed in-situ morphological and dynamic studies[28,29]. First, by using quantitative Grazing Incidence X-ray diffraction

(GIXD) analysis, we show that the molecular packing of P3EHT is dominated by the sulphur-containing backbone and that the diffraction pattern is only weakly dependent on the side chain carbons. From high-field ^{1}H double-quantum NMR analysis we show that the thiophene rings are titled with respect to the polymer main chain axis. Thus, on the basis of these experiments, we are able to validate the previously proposed packing motif for P3EHT in which adjacent molecular backbones have a difference in tilt angles[30]. Next, by applying various NMR methods, we demonstrate that the ethyl-hexyl side chains in P3EHT crystals are significantly mobile and most likely do not exhibit a fixed conformational state. Lastly, we present an Avrami-based model for capturing the crystallization dynamics of P3EHT in the solid state. Due to its relatively low melting temperatures, P3EHT crystallizes slowly at room temperatures when quenched to room temperature from the melt and allows for detailed, in-situ studies of the crystallization process. By fitting experimental absorbance and NMR data, we are able to set up a growth model and extract intrinsic crystallization parameters. The results as a whole represent an in-depth description of nucleation and crystallization of polythiophene crystals, the molecular packing structure of such crystals, and the dynamics of specific molecular segments within such structures. The methods presented here also provide a powerful set of tools for the characterization of semiconducting polymer crystals in general, which is able to capture long-range and molecular ordering effects.

2. EXPERIMENTAL SECTION

2.1 Materials

P3EHT (M_w = 7.5 kDa, M_n = 6.7 kDa, PDI = 1.11) were synthesized according to previous reports[28]. All other chemicals and solvents were purchased and used without further purifications.

2.2 Thin film preparations

Thin films of different thicknesses are fabricated by spin casting P3EHT solutions in hot (~80 °C) chlorobenzene with varying concentrations (5 to 40 mg mL−1) at 1200–1500 rpm for 1 min. Substrates for X-ray diffraction and optical absorption measurements are Si(100) wafers and plain glass slides, respectively. All substrates were solvent cleaned and treated with UV-ozone for 20 minutes prior to spin casting. Spin casting was performed in a N_2 glove box (< 10 ppm O_2) for all films. Film thicknesses are determined using a Veeco Dektak 150 profilometer.

2.3 Grazing Incidence X-ray Diffraction

Diffraction patterns are collected at beamline 11-3 at the Stanford Synchrotron Radiation Laboratory (SSRL) using an incident synchrotron X-ray beam of 12.7 keV at a grazing angle of 0.1°. The scattered intensities are recorded on a MAR-345 2D image plate and expressed as a function of the scattering vector $q = 4\pi\sin(\theta)/\lambda$ along q_{xy} and q_z. Here, θ represents half of the scattering angle, λ is the wavelength of the incident beam, q_{xy} is the component of the scattering vector parallel to the substrate plane and q_z is the component perpendicular to the substrate plane.

Crystallographic refinements were performed by integrating the diffraction intensities of various peak areas using the software WxDiff. The Monte Carlo optimization of the crystallographic residual was performed using an in-house software that optimizes the conformation of rigid dimers within the P3EHT unit cell in an attempt to obtain a best fit of the integrated peak intensities to the structure factor moduli (corrected for scattering geometry and beam factors). Details of the procedure are described elsewhere in literature[31,32].

2.4 UV-Visible Absorption

Films of different thicknesses for absorption experiments are fabricated on glass substrates. Spectra are obtained using a Varian Cary 6000i UV-Vis-NIR spectrophotometer and fitted to a modified Spano model to yield the percent aggregate, excitonic bandwidth W and average aggregate length l (see **Supporting Information section S.4**).

2.5 Solid-state NMR

^{13}C Solid-State NMR Spectroscopy: The cross-polarization magic angle spinning (CP/MAS) and 2D [1]H-^{13}C heteronuclear correlation (HETCOR) NMR experiments were performed at room temperature (295 K) on a 400 MHz Bruker AVANCE III spectrometer using a 4.0 mm MAS probe. The MAS frequency was 15.0 kHz and ^{13}C and [1]H 90°pulse lengths were 4.0 and 2.5 µs, respectively. The ^{13}C chemical shift was determined using the carbonyl peak at 175.6 ppm of glycine as an external reference with respect to tetramethylsilane (TMS). CP was achieved with ramped radio-frequency (RF) amplitude (80–100%) with contact time of 1 ms. SPINAL-64[33] heteronuclear decoupling was performed with 100 kHz decoupling frequency. Dipolar Chemical Shift Correlation

(DIPSHIFT) experiments were recorded at room temperature on a 400 MHz Varian UNITY INOVA NMR spectrometer, using a Jakobsen design 7 mm MAS probe. The MAS frequency was 6 kHz and ^{13}C and ^{1}H 90° pulse lengths were 4.5 and 4.0 μs, respectively. Cross polarization was achieved with ramped RF amplitude (80–100%) using a contact time of 0.5 ms. TPPM[34] heteronuclear decoupling and Frequency Switched Lee-Goldburg (FSLG) homonuclear decoupling[35,36] were performed with a decoupling frequency of 60 kHz. All high field ^{13}C solid-state NMR measurements were performed using 5s recycle delays at 310 K (corrected room temperature due to the heating friction caused by spinning the sample at 6 kHz).

^{1}H Solid-state NMR Spectroscopy: All solid-state ^{1}H MAS NMR experiments were performed on a 9.4 T (400 MHz for ^{1}H) spectrometer using a 2.5 mm Bruker probe operating in double-resonance mode. The magic angle setting was done on KBr and referencing of resonances was done relative to tetramethylsilane (TMS) using adamantane as a secondary reference with ^{1}H at 1.85 ppm[37,38]. All experiments employed a MAS frequency of 25.0 kHz and the carrier frequency was set to 3.00 ppm with all $\pi/2$ pulses lasting 2.6 μs. To reduce the ^{1}H background of the probe in the displayed ^{1}H MAS NMR spectrum, the procedure proposed by Chen *et al.* was invoked by subtracting an experiment using a π pulse (5.2 μs) and scaled by a half from an experiment using a $\pi/2$ pulse (2.6 μs)[39]. In both cases, the number of dummy scans and co-added scans extended over the entire four-step phase cycle. The relaxation delay was set to 4 s. The 2D ^{1}H-^{1}H double-quantum single-quantum (DQ-SQ) MAS NMR correlation experiment utilized the Back-to-Back (BaBa) recoupling sequence with two rotor periods DQ recoupling and DQ reconversion[40]. The dwell time in the indirect dimension was set to one rotor period. The number of dummy scans and co-added scans extended over the entire 16-step phase cycle and the relaxation delay was set to 3 s. A 2D rotor-encoded ^{1}H-^{1}H DQ-SQ experiment was performed to determine ^{1}H-^{1}H internuclear distances and thereby gain more insight into the packing of P3EHT[41]. This experiment was recorded using the broadband BaBa recoupling element[40] repeated three times to achieve DQ recoupling and reconversion for six rotor periods, respectively. The dwell time in the indirect dimension was set to 2.5 μs giving a total spectral width of 400 kHz. The number of dummy scans extended over the entire 16-step phase cycle and the full 2D spectrum was recorded using 940 increments in the indirect dimension for 64 scans with a relaxation delay of 3 s. The resulting NMR spectra were processed using Topspin 3.2. Phase correction was done

manually, and no line broadening was applied. The ^{1}H-^{1}H DQ sideband pattern for the thiophene proton in the indirect dimension was extracted as a summed projection between 4.2 and 10.4 ppm. All numerical simulations were performed using SIMPSON version 4.1.1[42,43]. The liquid-state ^{1}H NMR spectrum of P3EHT was acquired at 9.4 T (400 MHz for ^{1}H). P3EHT was dissolved in deuterated chloroform (CDCl$_3$) and referencing has been done relative to the residual solvent signal at 7.24 ppm. The experiment used two dummy scans and a total of 16 scans were acquired using an acquisition time of 4.1 s and a relaxation delay of 1 s.

^{1}H Time Domain NMR: Low-field time-domain NMR (TDNMR) measurements were performed on a 20 MHz Bruker MINISPEC. ^{1}H 90° pulse length was 2.5 μs. Recycle delays were typically 3s. The magic-sandwich echo (MSE) sequence[44] was used to produce dipolar refocused FIDs at echo times of 100 μs. Dipolar-filtered MSE experiments (DFMSE) were performed using a Goldman-Shen T$_2$-type filter[45] with a filter time of 40 μs. In the ^{1}H TD NMR experiments focusing on the recrystallization of P3EHT, thick P3EHT films were drop-casted onto cleaned glass substrates, mechanically removed, and packed into the NMR glass tube. The sample was melted inside the spectrometer above 80 °C and quenched to the crystallization temperature at a rate of 40 °C/min.

All NMR measurements were conducted using drop-casted P3EHT film samples (with thicknesses of approximately 1μm).

3.   RESULTS AND DISCUSSION

3.1   P3EHT Crystal Structure

The determination of the crystal structure for a semiconducting polymer has been shown to be possible via X-ray and/or electron diffraction experiments[30,31]. The material, however, must diffract and yield a number of diffraction spots higher than the total number of degrees of freedom for the unit cell. For P3EHT, the unit cell contains four ethyl-hexyl-thiophene monomers, a total of 52 atoms (ignoring hydrogen atoms) and thus would require a minimum number of 156 diffraction peaks given that each atom has 3 degrees of freedom. Previously, we were able to circumvent this stringent requirement by fixing the relative position of the carbon and sulfur atoms within a polymer backbone, removing all side chain carbons and only allow individual polymer chains within a unit

cell to slide and twist along the polymer backbone[30]. Here we would like to analyze the diffractive contributions of polymer side chains to the P3EHT thin film diffraction pattern.

In **Figure 1a**, we show a 2D Grazing Incidence X-ray Diffraction (GIXD) pattern for a P3EHT thin film (~15 nm) spin-cast on SiO_2. Based on a previously published unit cell for P3EHT (a = 7.72Å, b = 10.83 Å, c = 15.16 Å, α = 69.84°, β = 103.03°, and γ = 109.86°)[30], we assign families of diffracting peaks to their corresponding scattering intensities. We then extract the diffraction intensities for each peak, correcting for background scattering intensities and geometrical factors. The square root values of the diffraction intensities, which is proportional to the structure factor $|F_{hkl}|$, are then used to refine the crystal structure of P3EHT (more details on the procedure can be found in References [30–32]).
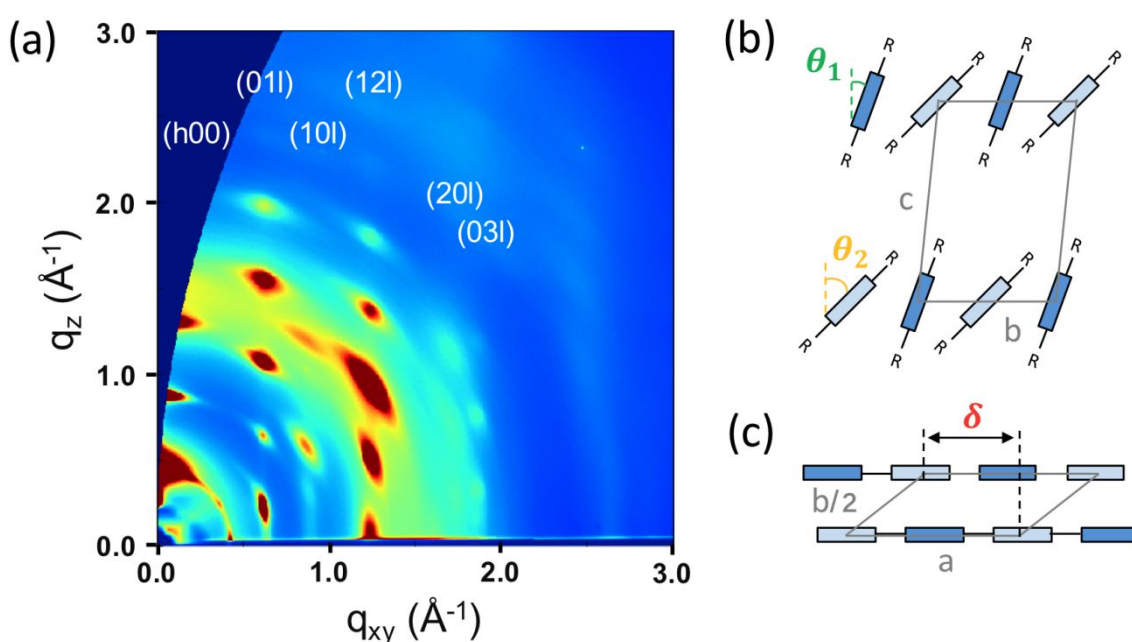
Figure 1. GIXD diffraction pattern for a ~15 nm P3EHT thin film (a) and schematic structures of the crystal structure viewed along the *a*-axis (b) and *c*-axis (c). R-groups in (b) represents the ethyl-hexyl aliphatic groups.

Unlike conventional refinements where the individual positions of each atom become parametric variables with respect to the unit cell dimensions and crystallographic space group, the determination of the P3EHT crystal structure performed here consists of only three parameters: the rotation angles of the backbone along the chain axis (θ_1 and θ_2) and the relative sliding distance between two adjacent polymer chains (δ) as shown in **Figure 1b** and **1c**. In other words, we place two thiophene dimers into each unit cell

with equal spacing along the *a*-axis and allow each chain to rotate and slide. For each different configuration, the refinement sequence calculates the expected diffraction intensities and iteratively minimizes the difference between calculated and measured diffraction intensities. The results show the structure with the lowest cost function (i.e. difference in diffraction intensities). Three independent runs of the refinement sequence were performed to ensure reproducibility. In order to predict the effects of the polymer side chains on the observed diffraction intensities, we used ten different starting thiophene dimers as inputs with varying side chain lengths and configurations. These different R-groups (**Figure 1b**) are summarized in **Figure 2** and include methyl (C1), ethyl (C2), propyl (C3), butyl (C4), 2-methylbutyl (C5), 2-ethylpentyl (C7) and 2-ethyl-hexyl (C8) group (two variants of C4 and C5 were used). Note, that these particular side groups were chosen to capture variations in the number of carbons and degrees of branching in addition to take into account different sidechain conformations. For C2-C8 this includes all-trans conformations for the methylene groups, whereas C4 and C5 also included all-trans and mixed trans-gauche sidechains. (see Supporting Information for structural files with exact atomic coordinates).
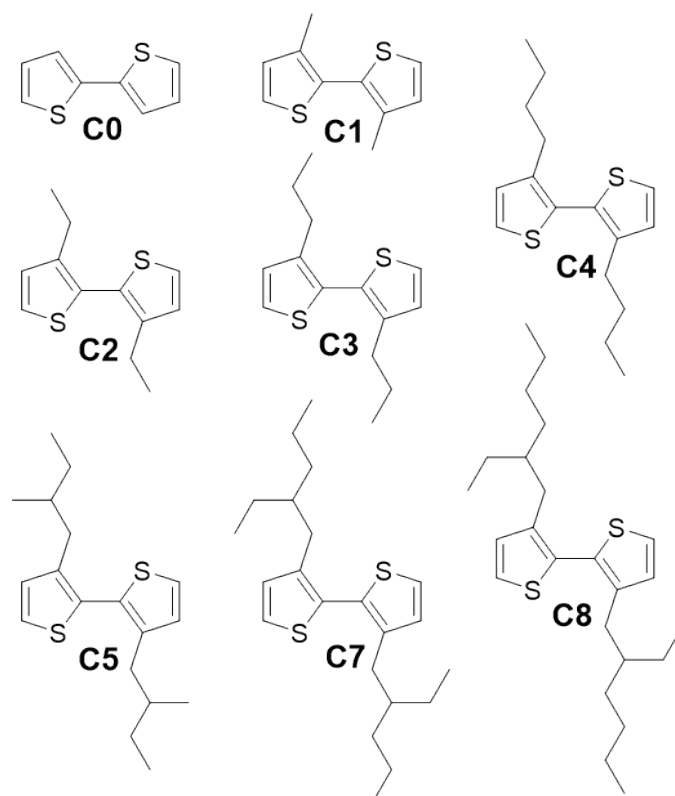
Figure 2. Chemical structures of different thiophene dimers used in the refinement of the P3EHT crystal structure. Note that the two alternate sidechain conformations for C4 and C5 are not shown (see Supporting Information for structural files with exact atomic coordinates).

The refinement results are summarized in **Table 1**. Here, $\Delta\theta$ represents the difference in tilt angles ($\theta_1 - \theta_2$) and the values obtained are directly generated from the refinements. The parameters denoted with an asterisk denote a symmetrically equivalent configuration of the final simulated state. The results show that the individual tilt angles of each chain do vary with the number of side chain carbons and configurations included in the simulations. There is not a monotonic trend, however, and the absolute angles vary between 17.8° to 46.2° for θ_1 and 1.4° to 19.3° for θ_2. Interestingly, the *differences* in tilt angles $\Delta\theta$ are fairly consistent across different input thiophene dimers and range from 14.6° to 31.4°. A similar trend is observed for the absolute sliding distance δ, which range from 1.80 to 2.25 nm. Finally, the cost function values are consistent across the three refinement runs for each thiophene dimer and decrease (i.e. improve) as more carbons are added from C0 to C4. Beyond this point, the cost function starts to increase again when going to longer side chains. It should be pointed out that the algorithm used for the crystallographic refinement does not check for atomic overlap and that significant overlap of the sidechains and neighboring polymer chains occurs for C5 to C8. Thus, the refinement was performed with fixed sidechain conformations and those structures where the overlap of the sidechains occurred were rejected. In summary, these results thus indicate that the conjugated polymer backbone dominates the scattering intensities for P3EHT, albeit with some contribution from the aliphatic carbons closest to the backbone. This result is of great importance for studying crystal structures of semiconducting polymer thin films, which are often weakly diffracting and do not exhibit enough diffracting peaks for large scale refinements. The same method of fitting the polymer backbone with minimal inclusion of side chain carbons is expected to be applicable to other polymer systems.

Table 1. Summary of the crystal structure refinement results.

R-group	θ_1 (deg)	θ_2 (deg)	δ (Å)	$\Delta\theta$ (deg)	θ_1^* (deg)	θ_2^* (deg)	δ^* (Å)	$\Delta\theta^*$ (deg)	Cost function (a.u.)
C0	-135.9	-347.2	1.61	211.4	44.1	12.8	-2.25	31.4	7.82E+06
C0	-135.9	12.8	1.61	-148.6	"	"	"	"	"
C0	224.1	12.8	1.61	211.4	"	"	"	"	"
C1	46.2	-161.3	1.84	207.4	46.2	18.7	-2.02	27.4	6.59E+06
C1	46.2	-161.3	1.84	207.4	"	"	"	"	"

R-group	θ_1 (deg)	θ_2 (deg)	δ (Å)	$\Delta\theta$ (deg)	θ_1^* (deg)	θ_2^* (deg)	δ^* (Å)	$\Delta\theta^*$ (deg)	Cost function (a.u.)
C1	46.2	-161.3	1.84	207.4	"	"	"	"	"
C2	-136.2	-344.4	-1.68	208.1	43.8	15.6	2.18	28.1	5.39E+06
C2	15.6	-136.2	1.68	151.9	"	"	"	"	"
C2	-136.2	15.6	-1.68	-151.9	"	"	"	"	"
C3	17.8	-144.5	1.67	162.3	17.8	35.5	-2.19	-17.7	5.21E+06
C3	-144.5	-342.2	-1.67	197.7	"	"	"	"	"
C3	17.8	-144.5	1.67	162.3	"	"	"	"	"
C4	-323.0	18.9	2.16	-341.9	37.0	18.9	2.16	18.1	4.91E+06
C4	18.9	-142.9	1.70	161.9	37.1	"	"	"	4.92E+06
C4	37.0	-341.1	2.16	378.1	37.0	"	"	"	4.91E+06
C4/2	-1.4	23.5	2.25	-24.9	23.5	-1.4	2.25	-24.9	5.70E+06
C4/2	-1.3	23.6	2.25	-24.9	23.6	-1.3	"	"	"
C4/2	23.6	-181.3	1.62	204.9	23.6	-1.3	-2.24	24.9	5.67E+06
C5	-131.4	-160.7	-2.06	29.3	48.6	19.3	-2.06	29.3	5.83E+06
C5	19.3	-131.4	-1.83	150.7	"	"	-2.03	"	5.87E+06
C5	-131.4	199.3	-2.05	-330.7	"	"	-2.05	"	5.83E+06
C5/2	-175.8	30.4	-1.62	-206.2	30.4	4.2	-2.24	26.2	5.47E+06
C5/2	30.3	4.1	-2.25	26.2	30.3	4.1	-2.25	26.2	5.48E+06
C5/2	-175.8	30.3	-1.62	-206.2	30.4	4.2	-2.24	26.2	5.47E+06
C7	13.5	-151.3	1.70	164.8	28.7	13.5	2.16	15.2	6.12E+06
C7	-151.3	13.5	-1.70	-164.8	"	"	"	"	"
C7	-346.5	208.7	1.70	-555.2	"	"	"	"	"
C8	12.0	-153.4	-1.73	165.4	26.6	12.0	-2.13	14.6	5.85E+06
C8	-348.0	-153.4	-1.73	-194.6	"	"	"	"	"
C8	-153.4	12.0	1.73	-165.4	"	"	"	"	"

*Symmetrically equivalent configuration of the final simulated state.

3.2. Molecular Packing of P3EHT from Solid-State ^{1}H NMR Spectroscopy.

To further characterize the molecular packing of the stacked polythiophene main chains of P3EHT we have taken advantage of a strategy that combines high-field ^{1}H liquid- and solid-state NMR spectroscopy. While liquid-state ^{1}H NMR spectroscopy inherently yields narrow and resolved ^{1}H resonances due to fast molecular tumbling in

solution, the spectral resolution in ^{1}H solid-state NMR experiments relies on fast magic-angle spinning (MAS). From such experiments utilizing fast MAS, it has been shown that the ^{1}H chemical shift is a sensitive probe with respect to π-π stacking and hydrogen bonding[46]. The effect of π-π stacking is observed as a shift of the ^{1}H chemical shift to either low- or high-field, depending on the aromatic or anti-aromatic character of the π-conjugated system[47,48], when compared to the corresponding liquid-state ^{1}H NMR signal. Moreover, solid-state NMR spectroscopy offers the possibility to detect and in some cases, also quantify the through-space [1]H-^{1}H inter-nuclear dipole-dipole coupling between π-stacked proton-bearing chemical groups from 2D NMR experiments, utilizing double-quantum (DQ) recoupling techniques[41,49–51]. This approach has been utilized for a variety of π-conjugated systems[52–55], where in particular the knowledge gained for donor-acceptor-based π-conjugated polymers has enabled unprecedented molecular insights about the donor-acceptor packing structure that is closely linked to the overall charge-transport properties[56–58].

We first characterize the ^{1}H NMR signal of P3EHT. **Figure 3** summarizes our results from liquid- and solid-state ^{1}H NMR spectroscopy. Based on previous NMR characterization of polythiophenes[59–61] it is straightforward to assign the liquid-state ^{1}H signal at 6.9 ppm in **Figure 3a** to the thiophene protons. From the corresponding ^{1}H solid-state NMR in **Figure 3b**, the thiophene protons are observed to resonate at 6.6 ppm with a significant increase in linewidth that is characteristic for ^{1}H resonances in the solid state[62]. This shows that the thiophene protons within the stacked P3EHT main chains are subject to a minor high-field shift of only ~0.3 ppm, which is indicative of weak to moderate π-π stacking effects. These observations are in good agreement with the relatively large, experimentally estimated π-π stacking distance of 5.08 Å from 2D GIXD in Section 3.1 (as calculated from the unit cell parameters $\frac{b}{2}\cos(\gamma - \pi)$). Moreover, it also demonstrates that the influence of aromatic ring currents from neighboring thiophene main chains on the ^{1}H chemical shift of the thiophene proton in P3EHT is fairly small compared to that of poly(3-hexylthiophene) or P3HT, where a π-π stacking distance of 3.9 Å for non-tilted thiophene main chains and high-field shifts of ~1.0 ppm for the thiophene protons have been reported[63].

To evaluate the spatial surroundings of the thiophene protons and further characterize the P3EHT crystal structure, we have recorded a 2D [1]H-^{1}H double-quantum single-quantum (DQ-SQ) spectrum as shown in **Figure 3c**. This spectrum was acquired

using a short DQ recoupling/reconversion time of 80 µs (two rotor periods) to probe the close spatial proton environment (below 5.0 Å)[64]. The 2D spectrum in **Figure 3c** includes clear cross-correlation signals between aromatic and aliphatic protons, occurring at the sum of the ^{1}H chemical shifts in the indirect ^{1}H-^{1}H DQ dimension (SQ$_1$+SQ$_2$=DQ; 0.8+6.6=7.4 ppm), in addition to two intense auto-correlation signals located at the spectrum diagonal. The auto-correlation signals are due to self-correlation between ^{1}H resonances with identical chemical shift as expected for the aliphatic signal at 0.8 ppm (CH$_2$ groups). The fact that the thiophene protons located at 6.6 ppm also display an auto-correlation signal demonstrate that the P3EHT main chains must be packed in such a way that the thiophene protons are in close registry. Though these findings seemingly contradict our previous statement on the limited π-π stacking, the short proton distances fit very well with the tilted polymer chain arrangement shown in **Figure 1b**, where limited conventional π-π stacking is present, explaining the high-field shift of only ~0.3 ppm. Increasing the DQ recoupling/reconversion time to 240 µs leads to a much less intense cross-correlation compared to the two auto-correlations at 0.8 and 6.6 ppm in the direct dimension (data not shown). This fact encouraged us to record a 2D rotor-encoded ^{1}H-^{1}H DQ-SQ spectrum in an attempt to quantify the ^{1}H-^{1}H internuclear distance between the thiophene protons. The resulting ^{1}H-^{1}H DQ sideband pattern encoding the ^{1}H-^{1}H thiophene-thiophene distance is displayed in **Figure 3d**. This spectrum was extracted from the full 2D rotor-encoded ^{1}H-^{1}H DQ-SQ spectrum as a summation over the region SQ=4.2 ppm to SQ=10.4 ppm, covering the thiophene-thiophene auto-correlation. Compared to a pure two-spin ^{1}H-^{1}H DQ sideband pattern, as recently observed for stacked perylene tetracarboxydiimide molecules with branched side chains[65], it is evident that the corresponding pattern for P3EHT in **Figure 3d** must be influenced by ^{1}H-^{1}H multi-spin effects as inferred from the signal intensities at even orders of the rotor frequency (marked by the symbol "#" in **Figure 3d**)[64]. This effect most likely is the result of the molecular packing of P3EHT main chains, which leads to a row (or one-dimensional chain) of coupled thiophene protons with varying inter-nuclear distances and proximities to the side chains. Nevertheless, we have as a first attempt assumed an ideal two-spin system. Through iterative fitting using SIMPSON[43,66], we obtained a ^{1}H-^{1}H thiophene-thiophene distance of 3.5±0.3 Å, corresponding to the simulated ^{1}H-^{1}H DQ sideband pattern (magenta) in **Figure 3d**. However, such a short distance is obviously too short and must reflect the multi-spin character of the ^{1}H-^{1}H DQ sideband pattern in **Figure 3d**, , i.e., the multi-spin character also changes the intensity distribution for the odd order ^{1}H-^{1}H dipolar

sideband pattern, leading to an overestimation of the ^{1}H-^{1}H dipolar coupling[67]. Thus, to analyze the ^{1}H-^{1}H DQ sideband pattern it is necessary to take into account the ^{1}H-^{1}H multi-spin effects and the approach we have taken is that of Zorin *et al.* based on the effective ^{1}H-^{1}H dipole-dipole coupling, or equivalent the effective distance, as a better measure to describe coupled ^{1}H-^{1}H networks[68]. The analysis is summarized in detail in the **Supporting Information Section S.1** and focuses on the relation between the effective thiophene-thiophene proton distances and the difference in tilt angle $\Delta\theta$ between pairs of successive thiophene main chains ($\theta_1 - \theta_2$) obtained from the crystallographic refinement (see **Figure 1b**). This analysis show that none of the structures from the crystallographic refinement produces an effective thiophene-thiophene proton distance that is short enough; the closest thiophene-thiophene distance is observed for C5 (3.88 Å) followed by C0 (3.91 Å). Correlating $\Delta\theta$ and the effective distance for all structures yields $\Delta\theta \sim 54°$ required for the short distance of 3.5 Å determined in **Figure 3d**. This angle is clearly not in agreement with the GIXD experiments above and may be considered as the upper limit for $\Delta\theta$, i.e., the thiophene-thiophene distance (dipole-dipole coupling) is underestimated (overestimated) due to multi-spin effects. Thus, the effective thiophene-thiophene distance measured from **Figure 3d** is on this basis estimated to be 4.0±0.3 Å (cf. Figure 31 in Ref. [64]). The analysis further indicates that difference in tilt angles $\Delta\theta$ between successive pairs of thiophene main chains is at least 15° and up to 50°, in agreement with the small high-field shift of ~0.3 ppm for the thiophene protons (**Figure 3**) and the results from GIXD (see **Figure 1b**)

Figure 3. (a) Liquid-state ^{1}H NMR spectrum and (b) solid-state ^{1}H MAS NMR spectrum of P3EHT recorded using a spinning frequency of 25.0 kHz. (c) 2D [1]H-^{1}H DQ-SQ spectrum of P3EHT recorded using two rotor periods of BaBa excitation and reconversion. Contour levels are displayed from 2.5% to 84% of the internal maximum. (d) Experimental [1]H-^{1}H DQ sideband pattern (black) recorded using six rotor periods of DQ recoupling/reconversion. The optimized simulation (magenta, shifted slightly to the left) is based on an ideal two-spin behavior and corresponds to a [1]H-^{1}H intermolecular distance of 3.5 Å. The [1]H-^{1}H multi-spin effects marked by # in (d) led us to use effective [1]H-^{1}H distances, resulting in an estimated, effective [1]H-^{1}H thiophene-thiophene distance of 4.0±0.3 Å, see text and Supporting Information for details. Green and magenta colors assign signals from the aliphatic ethyl-hexyl sidechain and the aromatic thiophene proton as shown in the inset of (a), respectively. The asterisks in (a) and (b) mark the residual solvent signal (CHCl₃) and an impurity, respectively.

Figure 3. (a) Liquid-state ^{1}H NMR spectrum and (b) solid-state ^{1}H MAS NMR spectrum of P3EHT recorded using a spinning frequency of 25.0 kHz. (c) 2D [1]H-^{1}H DQ-SQ spectrum of P3EHT recorded using two rotor periods of BaBa excitation and reconversion. Contour levels are displayed from 2.5% to 84% of the internal maximum. (d) Experimental [1]H-^{1}H DQ sideband pattern (black) recorded using six rotor periods of DQ recoupling/reconversion. The optimized simulation (magenta, shifted slightly to the left) is based on an ideal two-spin behavior and corresponds to a [1]H-^{1}H intermolecular distance of 3.5 Å. The [1]H-^{1}H multi-spin effects marked by # in (d) led us to use effective [1]H-^{1}H distances, resulting in an estimated, effective [1]H-^{1}H thiophene-thiophene distance of 4.0±0.3 Å, see text and Supporting Information for details. Green and magenta colors assign signals from the aliphatic ethyl-hexyl sidechain and the aromatic thiophene proton as shown in the inset of (a), respectively. The asterisks in (a) and (b) mark the residual solvent signal ($CHCl_3$) and an impurity, respectively.

3.3 Molecular Motions in P3EHT

Now that we have a good understanding of the polymer's backbone configurations and packing structure, we also want to know in more detail the polymer's chain mobility. As first hint about this issue we present the results of DSC measurements in **Figure 4a**. DSC trace shown in **Figure 4a** show three main thermal transitions. The peak at ~313 K might be related to a solvent-induced metastable phase and/or a glass transition temperature (since a slightly change of base-line seems to be happening at that region). The DSC trace also shows that melting peak is clearly split which was previously reported by Beckingham et al[69] in which the bimodal melting peaks T_1 and T_2 ($T_1 < T_2$) to the melting of crystallites formed during isothermal crystallization and those that were recrystallized and refined by the heating process, respectively. Note that the relative fraction of melted crystallites between T_1 to T_2 shown in **Figure 4a** is similar to that reported by Beckingham et al[69].
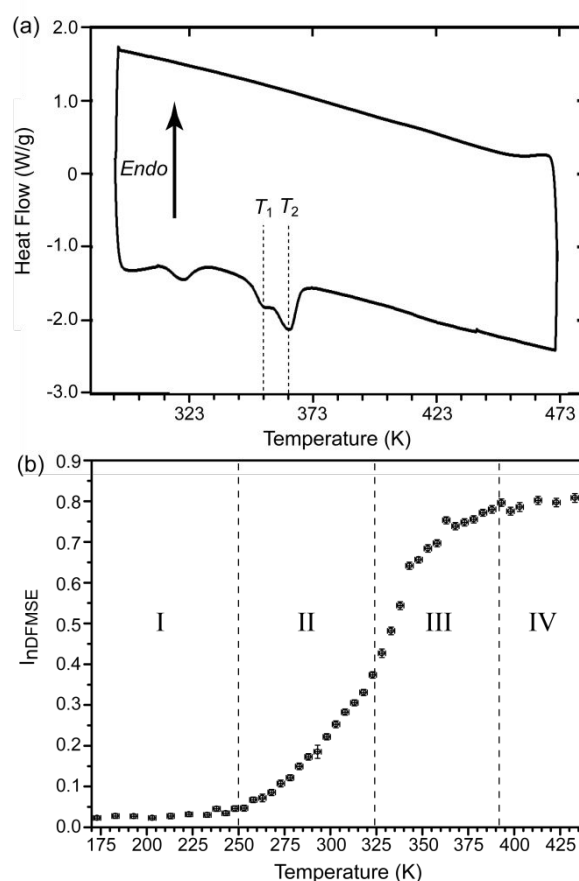
Figure 4. (a) DSC trace for P3EHT taken at a ramp rate of 10°C per minute. Note that no recrystallization events are shown due to the kinetically slow crystallization nature of P3EHT. (b) Normalized intensity of the ^{1}H DF-MSE TDNMR signals measured as a function of temperature for P3EHT using a filter time of 40 μs. The error bar at approximately 300 K is slightly bigger than the others due to the changing of cooling mechanism in our experiment (from blowing cooled N_2 to room temperature N_2).

DSC measurements can be effective for determining transition temperatures associated to global motions of the polymer chains, such as melting or glass transition processes. However, it usually fails in observing onset temperatures of local motions, such as end group or side-chain movements. This can be achieved using ^{1}H NMR because the [1]H-^{1}H dipolar coupling is highly sensitive to motion with rates higher than the dipolar coupling strength, which is usually in the in the order of tens of kHz for ^{1}H nuclei in rigid segments. Indeed, the changes in the [1]H-^{1}H dipolar coupling as a function of temperatures can provide the onset temperatures of thermally activated local or global movements of the polymer chains. This can be performed employing the so called ^{1}H TDNMR dipolar-filtered magic-sandwich echo (DF-MSE) measurements at low magnetic field. The DF-MSE experiment consists of a Goldmann-Shen type of dipolar filter with duration t_f[45], which suppresses ^{1}H signals whose decay time is faster than the filter time, followed by a mixed Magic Sandwich Echo sequence[70] (see **Supporting Information section S.3** for the pulse sequence). This is due to the stronger [1]H-^{1}H dipolar couplings in the rigid fraction, causing the NMR signals to decay in a time scale of about 40 µs. Thus, if the filter time t_f is longer than ~40 µs, the dipolar filter sequence suppresses signals arising from ^{1}H nuclei in rigid segments. In other words, the filter promotes a selection of the signal from mobile segments. Because the mixed-MSE sequence is able to refocus the signal of both rigid and mobile segments, at very short filter times t_f (~1 µs), the ^{1}H signal obtained after the DF-MSE sequence contains contributions from both rigid and mobile segments (**Supporting Information Section S.3**). If the filter time t_f is increased to values higher than ~40 µs, the ^{1}H signal arises only from mobile components. Notice that for a molecular segment to be seen as mobile in the DF-MSE experiments its motion rate should be higher than the inverse of the filter time, i.e., $k > 1/t_f$, which for typical filter time of 40 µs gives k > 20 kHz. Therefore, at very low temperatures where all molecular segments are rigid within this frequency scale, the corresponding ^{1}H signal will be completely suppressed and the intensity of the MSE echo will vanish. However, if the temperature is increased in such a way that the motion starts in some molecular segments, the dipolar filter sequence no longer suppresses the corresponding ^{1}H signal and the MSE echo appears. Thus, the method is able to detect the onset temperature of specific molecular motions as observed by an increase of the ^{1}H DF-MSE echo intensity as a function of temperature, which will be seen as an intensity upturn of the DF-MSE echo intensity vs. T curve, see **Supporting Information Section S.3**. It is worth mentioning

that the ^{1}H DF-MSE echo intensity is prone to temperature variations other than those caused by molecular motion, e.g. due to the temperature dependence of the magnetization (Curie law) or changes in the pulse and detection performance of the spectrometer. To normalize these effects, the ^{1}H DF-MSE echo intensity is divided by the intensity obtained at short filter time t_{f0}(~1 µs) providing a normalized ^{1}H DF-MSE intensity, $I_{nDFMSE} = \frac{I_{DFMSE}(t_f)}{I_{DFMSE}(t_{f0})}$, in which the variations are expected to be only related to molecular motions. Note also that at temperatures were the motional rates becomes comparable to the dipolar coupling frequency, (intermediate motion regime), the MSE intensity is reduced. However because the same MSE is used for acquiring both $I_{DFMSE}(t_f)$ and $I_{DFMSE}(t_f)$ intensity this effect is also normalized out in I_{nDFMSE}. In summary, an intensity upturn of the I_{nDFMSE} vs. T curve is directly related with the onset of molecular motions in some segments in the sample. A more complete description of the DF-MSE experiment can be found in the **Supporting Information Section S.2**.

The I$_{DFMSE}$ vs. T curve measured for P3EHT is shown on **Figure 4b**. This curve was obtained by recording ^{1}H DF-MSE echoes using filter times t$_f$ of 1 µs and 40 µs, respectively, as a function of temperature. The intensities $I_{DFMSE}(t_{f0} = 1µs)$ and I_{DFMSE} $(t_f = 40µs)$, obtained as the maximum intensity of those echoes, are then used to provide the normalized $I_{nDFMSE} = \frac{I_{DFMSE}(t_f = 40µs)}{I_{DFMSE}(t_{f0} = 1µs)}$ for each temperature. Three temperature regions can be identified in the curve. Region I, below 250 K, comprises the temperature where there is no motions in the frequency scale of DF-MSE, so $I_{nDFMSE} = 0$. Region II, from 250-325 K, correspond to temperature range between the first and the second intensity upturn. The ^{13}C{^{1}H} CP/MAS build up, dipolar-dephased ^{13}C{^{1}H} CP/MAS and ^{13}C T_1 relaxation time experiments, **Supporting Information Section S.2,** suggested that at 310 K the thiophene main chain is quite rigid while side-chains have the highest mobility. Therefore, the changes in the I_{nDFMSE} in this region can assigned predominantly to side-chain motions. As for region IV, the DSC traces shown in **Figure 4a** suggests that the melting of the crystallites is completed. Therefore, region IV corresponds to the melt state and I_{nDFMSE} remain constant as expected. The assignment of the processes associated to region III is rather more complicated. In this region the reducing of the ^{1}H-^{1}H dipolar coupling contribution can be attributed to motions associated to the melting of the solvent-induced metastable phase and/or a glass transition temperature, at ~313 K

according to the DSC results and Beckingham et al[69], and also to the melting of the crystallites at 340-370 K according to the DSC traces.

Although the DSC and ^{1}H DF-MSE bring information about onset temperatures of molecular motions, they do not provide molecular details of the such motions. In particular, we are interested in molecular mobility of the side chains in relation to the backbone. We have chosen ^{13}C solid-state NMR spectroscopy as the method of choice for this investigation. The short-ranged nature and orientation dependence of the nuclear spin interactions make solid-state NMR sensitive to the packing and conformation of chains in crystalline and amorphous domains and also to segmental molecular motions.

Figure 5a shows the ^{13}C{^{1}H} CP/MAS NMR spectrum acquired for P3EHT. Signals in the 120-140 ppm and 5-45 ppm spectral ranges are associated with the polythiophene main-chain and side-chain carbons, respectively. The assignment of the signals to specific carbons of the P3EHT chemical structure shown in **Figure 5a** was done using a combination of short recycle delay direct polarization (^{13}C DP MAS NMR), dipolar-dephased ^{13}C{^{1}H} CP/MAS NMR, and 2D ^{13}C-^{1}H heteronuclear correlation experiments (2D ^{13}C-^{1}H HETCOR NMR). Detailed results and discussions that lead to the assignments can be found in **Supporting Information Section S.2**.
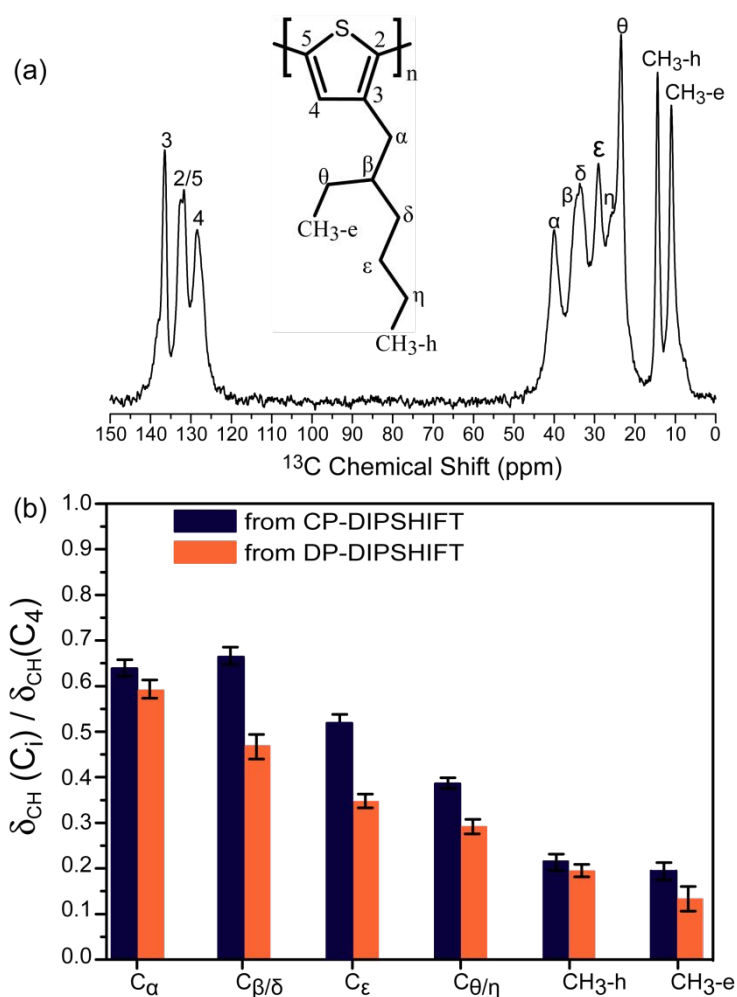
Figure 5. (a) $^{13}C\{^1H\}$ CP/MAS NMR spectrum and signal assignments for P3EHT. The inset presents the P3EHT chemical structure with labels assigned to each carbon in the molecule. Detailed results that lead to the assignments and corresponding discussions are presented in the Supporting Information Section S.2. (b) Bar graph of the $\delta_{CH}(C_i)/\delta_{CH}(C_4)$ ratios extracted from the DIPSHIFT curves for several protonated sidechain carbon sites of P3EHT, where the index i corresponds to each protonated carbon site of the sidechain.

It is well-known that the side chain mobility in polymer can influence the molecular packing, mechanical and thermal behavior as well as the material processability. Information about the molecular mobility of specific carbon sites was obtained using the *Dipolar Chemical Shift Correlation* (DIPSHIFT)[71] experiment. The DIPSHIFT experiment provides a measure of the strength of the magnetic dipolar coupling between ^{13}C bonded to ^1H nuclei (C-H coupling, δ_{CH})[72]. Since the strength of the C-H coupling is reduced due to molecular motions with rates between (10-100 kHz)[73–76], DIPSHIFT experiments are capable of probing molecular dynamics within this frequency window[77,78]. This is provided by a pulse sequence (see **Supporting Information Section S.2**) that modulates the intensity of each line of the $^{13}C\{^1H\}$

CP/MAS NMR spectrum by the local C-H couplings, which are then quantified by measuring the resonance intensities as a function of an experimentally incremented evolution time t_1 (DIPSHIFT dephasing curves, see **Figure S6** in the **Supporting Information Section S.3**). The molecular mobility information is summarized by the reduction of δ_{CH} due to motion. This is usually probed by DIPSHIFT using the so called dynamical order parameter, which is defined as the ratio between the strength of the motion reduced C-H coupling without the influence of the molecular motion (rigid limit CH-coupling), see more detailed discussion in the **Supporting Information Section S.3**). Despite this gives an absolute measurement to the degree of mobility, it requires the measurement of rigid limit CH-coupling, which is done by acquiring the DIPSHIFT curve at rather low temperatures or for a standard sample where there is no motion in the kHz frequency scale. However, while in the first approach is more prone to errors due to differences in the efficiency of the homonuclear decoupling at different temperatures, in the second approach the errors can arise from structural differences between the standard and the actual sample[79]. Thus, because at room temperature the P3EHT is below its glass transition temperature [69], we expect the PEHT backbone to be rigid. Thus, we use the δ_{CH} measured via DIPSHFIT of the C4 carbon (the only protonated carbon in the backbone) as an internal reference to normalize the δ_{CH} values obtained for the others side-chain carbons. This gives the ratio $\delta_{CH}(C_i)/\delta_{CH}(C_4)$ which reflect the mobility difference between each side-chain carbon and the backbone, i.e., the smaller is $\delta_{CH}(C_i)/\delta_{CH}(C_4)$ the more mobile is the that specific segment relative to the backbone. Because the δ_{CH} values are extracted from a single DIPSHIFT measurement at the same conditions this ratio is less prone to the aforementioned errors but is only gives a measurement of the relative mobility between the side-chain and the backbone. More details regarding the DIPSHIFT pulse sequence and corresponding parameters, see **Supporting Information Section S.3**.

Figure 5b shows the $\delta_{CH}(C_i)/\delta_{CH}(C_4)$ ratios determined from the DIPSHIFT dephasing curves for each resolved protonated carbon site of P3EHT. Two excitation methods, cross-polarization (CP) and direct polarization (DP), were used to record the DIPSHIFT curves. Fits to the dephasing curves, from which the $\delta_{CH}(C_i)/\delta_{CH}(C_4)$ ratios were calculated, are shown in **Figure S7** in the **Supplementary information section S.3**.

With respect to the ethyl-hexyl side-chain motion, all side-chain carbons exhibited $\delta_{CH}(C_i)/\delta_{CH}(C_4)$ ratios significantly smaller than 1. There is an evident decrease of the order parameter along the side-chain, with higher $\delta_{CH}(C_i)/\delta_{CH}(C_4)$ ratios being observed for those carbon sites close to the thiophene main chain (C_α and C_β) and lower values for carbons sites near the end of the side-chain. This results of a typical gradient of mobility (heterogeneity in the amplitude of the motion) throughout the side-chain observed for polymers with rigid backbone and mobile side chains[74,75]. The presence of such a gradient of mobility can be taken as evidence that the side-chain motion is not isotropic, but occurs around a local side-chain axis, with some extra degrees of freedom for the end side-chain groups likely encouraged by branching of the ethyl-hexyl group. Note also that in the $^{13}C\{^1H\}$ CP/MAS NMR spectra in **Figure 5a** the side-chain signals are broader for carbons closer to the main chains, which is also in agreement with the presence of a mobility gradient. As already mentioned, this picture agrees with the correlation signal observed in 2D ^1H-^1H DQ-SQ spectrum, which close spatial proximity, between the thiophene proton and the first aliphatic groups of the ethyl-hexyl sidechain.

3.4   Crystal Growth Based on an Extended 1D Avrami Model

Previously, we have shown that crystallization of P3EHT thin films is dominated by growth along a single direction: the chain axis/polymer backbone direction[80]. This was confirmed by the relatively fast crystal growth of P3EHT along the π-stacking and alkyl-stacking directions as observed from GIXD. Crystallization kinects has been well studied using the well-known Avrami Model, which considers crystal to grow isotopically in a three-dimensional fashion. Given that crystallization of P3EHT thin films is proved to be purely one-dimensional, we had to modify the form of the Avrami model to fit time-dependent crystallization curves. Using an extended form of the Avrami model to fit time-dependent optical absorption data, as is shown below in **Equation (1)**, we were also able to capture the rate (k) and dimensionality (n) of the crystallization process[80].

$$A = A_g\left(1 - \exp\left(kt^n\right)\right) + A_o \tag{1}$$

Here A represents the total fraction of aggregates, A_o is the initial fraction of aggregates ($t = 0$) and A_g is the fraction of aggregates gained at long times (the sum of A_o and A_g is the final aggregate fraction after crystallization has completed). For 1D growth, the dimensionality factor n is between 1 and 2, where a value of 1 represents fast nucleation and a value of 2 represents slow nucleation. This form of the Avrami model, however,

does not allow for easy comparisons between data sets due to the fact that n is almost always different. In other words, different growth rates k cannot be compared when n is not constant. We now present a more in-depth form of the Avrami model that takes into account the size and growth mechanism observed.

Firstly, we consider the fundamental basis for the Avrami model, which proposes that there exists a certain density of nucleation sites (N) within the solid-state of a particular crystallizing system. Each nucleation site has a probability of nucleating into a crystal, which is described by the nucleation rate v_N (i.e. the number of nucleation sites that nucleate per minute). **Equations (2-4)** describe below the available number density of nucleation sites (N) at a particular point in time. Here N_o describes the initial density of available nucleation sites at $t = 0$ (i.e. the total density of nucleation sites).

$$dN = -N * v_N * dt \tag{2}$$

$$\int_{N_o}^{N} \frac{dN}{N} = \int_0^t - v_N * dt \tag{3}$$

$$N(t) = N_o\exp\left(-v_N t\right) \tag{4}$$

Based on these equations, we can now calculate the volumetric rate of nucleation I_v, which defines the average number of aggregates that nucleate per unit volume per minute, as:

$$I_v(t) = -\frac{dN}{dt} = N_o v_N \exp\left(-v_N t\right) \tag{5}$$

Once a crystal has nucleated, it grows at a constant rate. For our current polythiophene system, the crystallizing species is a π-stacked *aggregate*, as was previously defined[20]. From diffraction data, the width and height of each aggregate are known to be around 6 nm along the π-stacking direction (w) and 1.45 nm along the alkyl-stacking direction (h), respectively. We assume that each nucleation site nucleates into a fully grown "rectangular" aggregate that grows along the aggregate length (l) at a constant rate L (**Figure 6**).
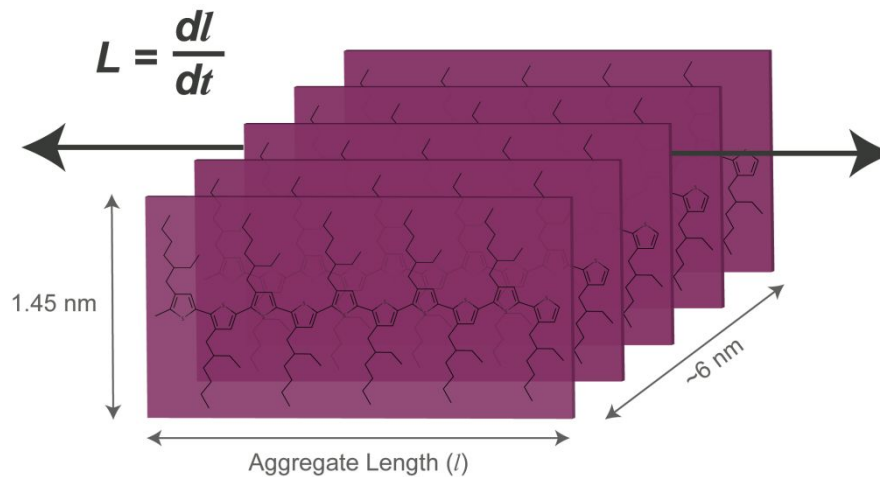
Figure 6. Schematic of an aggregate and its 1-D growth along the thiophene backbone.

The volumetric growth rate $\left(\frac{dV}{dt} \right)$ of a single aggregate can then be defined as follows:

$$V_S = h * w * l \tag{6}$$

$$\frac{dV_s}{dt} = h * w * \frac{dl}{dt} \tag{7}$$

We can then define the volume of a particular aggregate that nucleated at time τ at any point in time t, as is defined below:

$$\int_\tau^t dV_s = \int_\tau^t h * w * L * dt \tag{8}$$

$$V_s(t) = hwL(t - \tau) \tag{9}$$

Now we consider the fact that the Avrami model assumes that each aggregate grows as if the other were not there; in other words, they will "overlap" with each other and are not affected by any impingements. The sum of all of the individual aggregate volumes is denoted as the *effective aggregate volume* (V_e^A) and includes the overlap volume. We can then define the change in V_e^A for an aggregate that nucleated at time τ as:

$$dV_e^A = v_N * I_v(\tau) * V_{tot} * d\tau \tag{10}$$

Note that $I_v(\tau) * V_{tot} * d\tau$ simply represents the number of aggregates that have nucleated between time τ and $\tau + d\tau$. Integrating this expression eventually yields the V_e^A as a function time (**Equation (12)**):

$$\int_0^{V_e^A} dV_e^A = hwLN_o v_N V_{tot} \int_0^t \exp\left(-v_N\tau\right) * (t - \tau)d\tau \tag{11}$$

$$V_e^A = \frac{hwLN_o V_{tot}}{v_N} [\exp\left(-v_N t\right) - 1 + v_N t] \tag{12}$$

Lastly, we want to calculate the real total *aggregate volume* (V^A) that does not include the virtual, overlap volume. This is done by considering that only a fraction of

the change or increase in V_e^A is "real" and is defined by the volume fraction of the solid that has not yet crystallized or transformed:

$$dV^A = \left(1 - \frac{V^A}{V_{tot}}\right)dV_e^A \tag{13}$$

By integrating **Equation (13)**, we calculate the overall fraction of aggregates (A):

$$\int \frac{dV^A}{\left(1 - \frac{V^A}{V_{tot}}\right)} = \int dV_e^A \tag{14}$$

$$A = \frac{V^A}{V_{tot}} = 1 - \exp\left(-\frac{V_e^A}{V_{tot}}\right) \tag{15}$$

Combining **Equation (12)** into **Equation (15)** yields the final expression for the fraction of aggregates:

$$A = 1 - \exp\left(-\frac{hwLN_o}{v_N}[\exp(-v_Nt) - 1 + v_Nt]\right) \tag{16}$$

As a check, we consider the extreme cases for very fast and very slow nucleation. For slow nucleation rates, $v_Nt \ll 1$ and A can be approximated using a Taylor series expansion as:

$$\exp(-v_Nt) = 1 - v_Nt + \frac{v_N^2t^2}{2}... \tag{17}$$

Taking the first three terms of the series in **Equation (17)**, the fraction of aggregates yields the following:

$$A = 1 - \exp\left(-0.5hwLN_ov_Nt^2\right) \tag{18}$$

For fast nucleation rates, $v_N \gg 1$ and A can be reduced to **Equation (19)**:

$$A = 1 - \exp\left(-8.7LN_ov_Nt\right) \tag{19}$$

These expressions match the standard Avrami exponential dependencies of $n = 1$ and $n = 2$ for fast and slow nucleation rates, respectively. Finally, we modify **Equation (16)** to account for the fact that polymer films cannot become 100% aggregated and may begin crystallization with a starting aggregate fraction. In **Equation (20)**, we have thus included the parameters A_o (the initial fraction of aggregates) and A_g (the fraction of aggregates gained at long times) as was previously explained:

$$A(t) = A_g\left[1 - \exp\left(-\frac{hwLN_o}{v_N}[\exp(-v_Nt) - 1 + v_Nt]\right)\right] + A_o \tag{20}$$

Using **Equation (20)**, which is the extended Avrami model for the present case, we can now analyze kinetic properties of crystallization and growth in solid-state P3EHT polymer samples. Note that for P3EHT the product hw is equal to 8.7.

3.5   Recrystallization Kinetics and Molecular Rearrangement of P3EHT probed by Solid-State NMR Experiments.

It is well known that ^{13}C solid-state NMR, in particular $^{13}C\{^1H\}$ CP/MAS NMR experiments, is highly sensitive to the local chain conformational in polymers[81]. Thus, the technique can be used as an effective way of probing polymer crystallization provided that the crystallization time is longer than the time required for the signal acquisition[82–85]. For P3EHT this is the case since the crystallization time may be longer than 12 h (depending on the crystallization temperature) and a $^{13}C\{^1H\}$ CP/MAS NMR spectrum with a reasonable signal-to-noise ratio can be acquired within ~1 h.

Figure 7a shows the series of $^{13}C\{^1H\}$ CP/MAS NMR spectra acquired in blocks of 2h during the crystallization at 30 °C, after having melted the P3EHT sample inside the NMR rotor and quenching to 30 °C at a rate of 40 °C/min. In the first 2h, ^{13}C signals from the thiophene carbons are featureless, indicating a high degree of conformational disorder[81]. Therefore, P3EHT is mostly in the amorphous state within this first 2h. For longer crystallization times, the emergence of narrow signals in the region of thiophene carbons indicates an increase in conformational order due to crystallization. As displayed in **Figure 7a**, crystallization is completed after 10h. By plotting the ^{13}C signal intensity associated with one of the thiophene carbons, for instance C_4 (see **Figure 4**), as a function of crystallization time, one can follow the crystallization kinetics. This is shown in **Figure 7c**, where the C_4 peak intensity was measured for each 1h of spectrum acquisition. The peaks associated with C2/5 and C3, depict the same trend, see **Figure S10** of the **Supporting Information Section S.3**.

Another interesting feature to be observed in the $^{13}C\{^1H\}$ CP/MAS NMR spectra of **Figure 7a** is associated with the side-chain carbons. The Cα signal follows the same behavior of the thiophene carbons, showing that crystallization also imposes local conformational ordering to the side-chains. However, as also shown in **Figure S10** of the **Supporting Information Section S.3**, the signals associated with the end ethyl-hexyl side-chain carbons, i.e., C_δ, Cε, Cη, C_θ and CH_3 are less affected by the crystallization. This observation suggests that crystallization makes the side-chains carbons close to the thiophene main chain more rigid in the crystallites, while the side-chain ends remain more mobile. This is in perfect agreement with the DIPSHIFT and shows that the strong correlation peak between aliphatic and aromatic protons in the 2D ^1H-^1H DQ-SQ correlation NMR experiments in **Figure 3c** is mainly a result from the strong ^1H-^1H

dipolar interaction, and thereby close spatial proximity, between the thiophene proton and the first aliphatic groups of the ethyl-hexyl side-chain. Moreover, the fairly high order parameter for the thiophene C4 position in combination with the decrease of the order parameter along the ethyl-hexyl side-chain observed from the DIPSHIFT experiments is characteristic of well-ordered and crystalline P3EHT domains as discussed above.

Although one can follow the crystallization kinetics using $^{13}C\{^{1}H\}$ CP/MAS NMR, the inconvenience of doing so is the long 1-hour acquisition time to obtain a $^{13}C\{^{1}H\}$ CP/MAS NMR spectrum with sufficiently and fair signal-to-noise ratio. On the other hand, the reduction in the mobility observed for some of the segments in the ethyl-hexyl side-chains upon crystallization suggests that the process could be probed by monitoring the overall mobility of the polymer chains, which can be achieved using ^{1}H TD-NMR. To demonstrate this concept, **Figure 7b** shows two MSE refocused ^{1}H MSE-refocused FIDs[70] measured for the same P3EHT sample before (0h) and after recrystallization (12h) at 30 °C. The decrease in decay time clearly shows the reduction of the proton mobility in the sample upon recrystallization. To probe the proton mobility reduction more specifically, the ^{1}H DF-MSE method was used. As already stated above, the ^{1}H DF-MSE experiments filters out ^{1}H signals for which the decay time is shorter than the filter time t_f. The decay time of ^{1}H signals arising from protons in rigid segments is about 30 μs. Thus, by setting t_f to 40μs, the intensity of the ^{1}H DF-MSE echo I_{DFMSE} ($t_f = 40$μs) will arise from protons in segments faster than this cut-off time only. Because all protons contribute to the intensity at short filter times I_{DFMSE} ($t_f = 1$μs), the normalized intensity that account for the fraction of rigid protons in the sample (in the sense of the ^{1}H DF-MSE experiment) reads

$$f_{rigid} = \frac{I_{DFMSE}(t_f = 1\mu s) - I_{DFMSE}(t_f = 40\mu s)}{I_{DFMSE}(t_f = 1\mu s)} \qquad (21)$$

As shown in **Figure 7b**, the number of rigid protons during the crystallization increases, so f_{rigid} should increase accordingly. Indeed, if the increase in f_{rigid} really probes the crystallization dynamics one should expect that the increase in the chain ordering, as probed by the intensity of the C_4 carbon in the $^{13}C\{^{1}H\}$ CP/MAS NMR experiment, and the change in f_{rigid} as a function of the crystallization time coincide. This hypothesis is borne out in **Figure 7c** where both quantities are plotted together as a function of the crystallization time. The agreement between both curves is remarkable,

demonstrating that f_{rigid} is an equally good probe of crystallization kinetics. In addition, since the two ^{1}H DF-MSE experiments required to evaluate f_{rigid} take only about 5 minutes, the crystallization kinetics can be probed with a much higher time resolution using ^{1}H DF-MSE, so the crystallization behavior can be followed in more detail.

Figure 8 shows the fraction of rigid ^{1}H as a function of crystallization time, $f_{rigid}(t)$ for recrystallization temperatures T_q of 30°C, 40°C and 50°C. As expected, $f_{rigid}(t)$ increases over time with an average rate of crystallization that decreases with increasing T_q. Recrystallization takes, for instance, only ~20 hours to complete at 30°C compared to the 120+ hours required for $T_q = 50°$C.
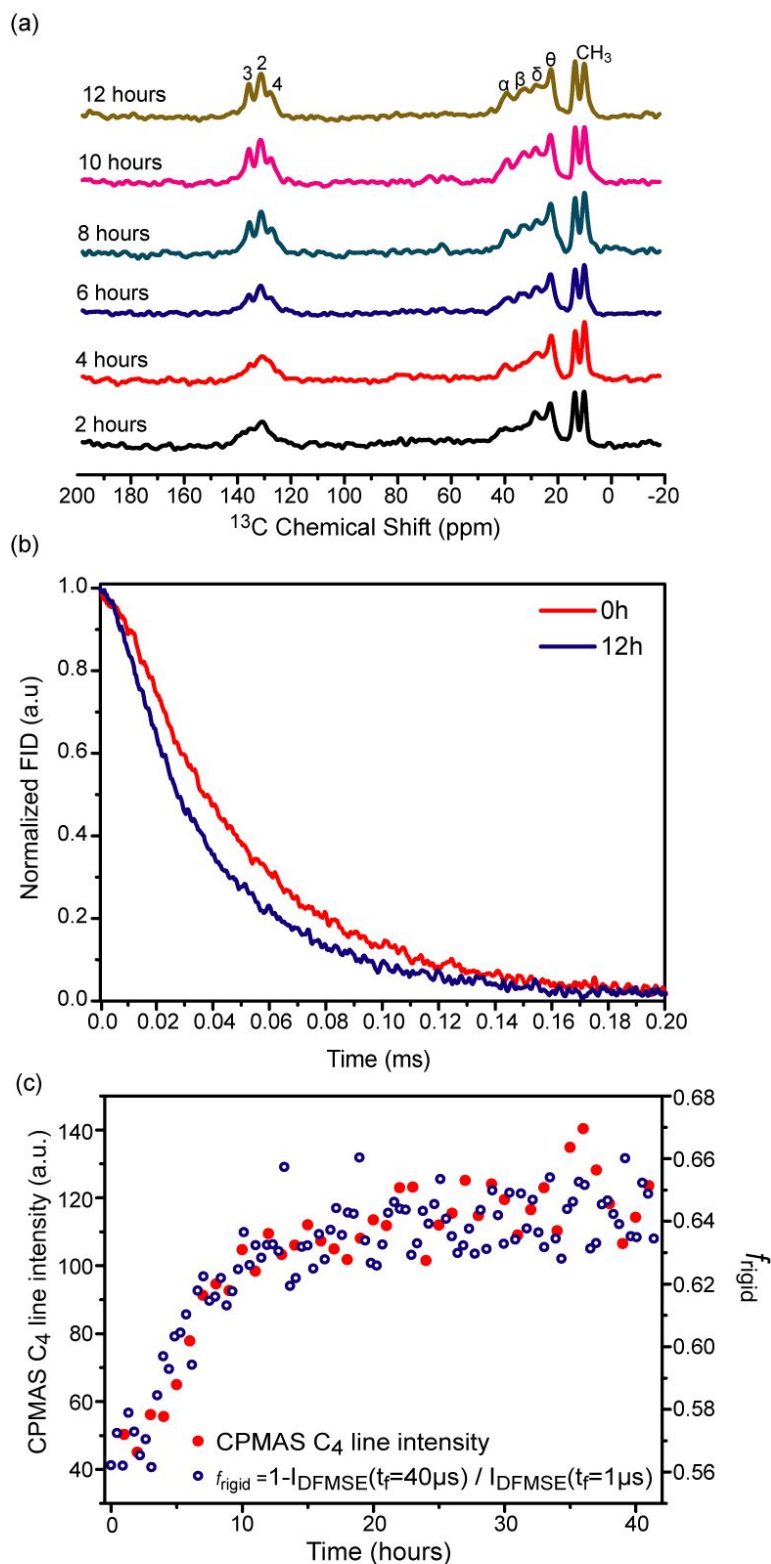
Figure 7. (a) $^{13}C\{^{1}H\}$ CP/MAS NMR spectra recorded during the crystallization of P3EHT for the indicated times. (b) Changes of the ^{1}H TDNMR FID due to the crystallization of P3EHT. (c) Comparison between the intensity of the C4 line in the $^{13}C\{^{1}H\}$ CP/MAS NMR spectrum and f_{rigid} extracted from the ^{1}H DF-MSE experiment during the crystallization of P3EHT for the indicated times.

3.6 Application of the Extended 1D Avrami Model to the Crystallization of P3EHT as Followed by ^{1}H Time-Domain and Optical Absorbance Experiments.

The possibility of probing the crystallization kinetics by monitoring $f_{rigid}(t)$ as a function of the recrystallization time has made it possible to test the validity of the extended 1-D Avrami model applied to the crystallization of P3EHT using the ^{1}H TDNMR results. Despite the fact that $f_{rigid}(t)$ probes the time dependence of the crystallization, the term inside the square bracket in **Equation 20,** the initial and asymptotic values of A, A_o and A_g, do not have the same meaning for the initial and asymptotic values of $f_{rigid}(t)$, named here as f_g and f_0. However, as already shown, aggregation is directly linked to the increase of $f_{rigid}(t)$, which means the f_g and f_0 should be proportional to A and A_o, respectively. Thus, the NMR equivalent of **Equations 1 and 20** are, respectively:

$$f_{rigid}(t) = f_g\left(1 - \exp\left(kt^n\right)\right) + f_o \tag{22}$$

and

$$f_{rigid}(t) = f_g\left[1 - \exp\left(-\frac{hwLN_o}{v_N}[\exp\left(-v_Nt\right) - 1 + v_Nt]\right)\right] + f_o \tag{23}$$

where k, n, L, N_o and v_N have the same meaning as before. Thus, it is possible using **Equations 22 and 23** to fit the experimental $f_{rigid}(t)$ curves and extract the characteristic crystallization parameters.
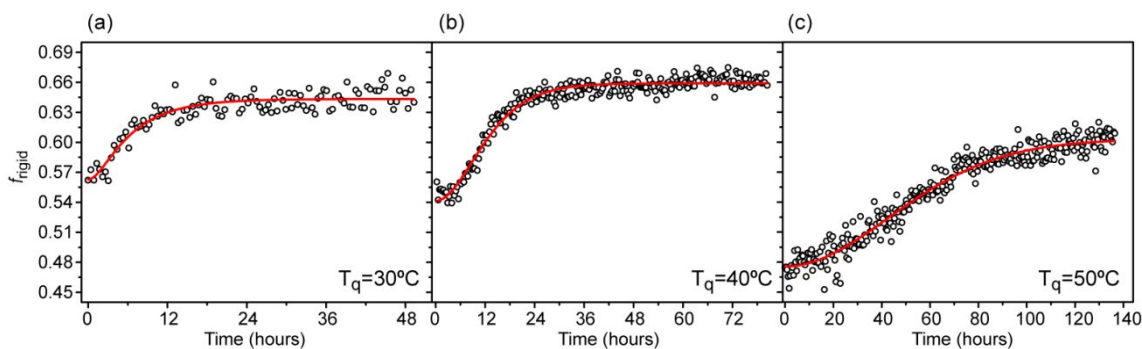
Figure 8. Plots of the normalized ^{1}H DF-MSE intensities acquired using the ^{1}H DF-MSE experiments (see **Equation 21**) for P3EHT as a function of time after being quenched from the melt to (a) 30 °C (b), 40 °C and (c) 50 °C. Red lines represent fits to the extended 1D Avrami model, see **Equation 22**.

To first validate that the crystallization is indeed 1D, we have fitted the NMR data with the traditional Avrami model as described in **Equation 22** (or **Equation (1) equivalent)** as summarized in **Table 2**. The comparison between the fitting using the

extended and traditional Avrami models are shown in **Figure S12** of **supplementary information section S.5**. The dimensionality factors n are determined to be 1.21, 1.87 and 1.94 for T_q of 30°C, 40°C and 50°C, respectively (**Table 2**). As expected for 1D growth, these n values are found to be between 1 and 2. Interestingly, n is close to 2 at 50°C, suggesting that the crystallization dimensionality may be approaching 2 close to the melting point of the polymer ($2 < n < 3$).

Applying the extended 1D Avrami model to fit the normalized ^{1}H TD-NMR data yields interesting dynamic properties for the recrystallization process. The nucleation rate v_N is found to vary between 7.80 x 10^{-5} to 9.38 x 10^{-3} min^{-1}. These correspond to average nucleation times, representing the time it takes for a nucleation site to develop a nucleus that is capable of growing into a crystallite, between 2 to 54 hours. The product of L, the aggregate extension rate (nm/min), and N_o, the total density of nucleation sites (nm^{-3}), is found to vary between 2.30 x 10^{-4} and 3.34 x 10^{-4} min^{-1} nm^{-2}. As will be later shown for P3EHT thin films, values for L are expected to be around ~0.1 nm/min, which results in values for N_o between 10^{-4} and 10^{-3} nm^{-3}. In other words, there is a nucleation site every 1,000 to 10,000 nm^3 (cubical areas with edges between 10-22 nm).

Table 2. Summary of the Avrami fitting results.

T_q (°C)	Simple Avrami				Extended 1D Avrami			
	f_g	k (min^{-n})	n	f_0	f_g	LN_0 (nm^{-2})	v_N (min^{-1})	f_0
30	0.08	6.03 x 10^{-4}	1.21	0.55	0.08	3.34 x 10^{-4}	9.38 x 10^{-3}	0.56
40	0.11	3.02 x 10^{-6}	1.87	0.54	0.11	3.18 x 10^{-4}	1.29 x 10^{-3}	0.54
50	0.12	1.13 x 10^{-7}	1.94	0.47	0.12	2.30 x 10^{-4}	7.80 x 10^{-5}	0.47

We now look at P3EHT thin films of different thicknesses spin-cast on glass, which have subsequently melted at 80°C and then recrystallized at room temperature (25°C). By measuring optical absorption spectra for each film as a function of time after quenching and fitting each spectrum using the H-aggregate Spano model[86,87], we can extract the film's fraction of aggregates and the aggregate length as a function of time using previously published methods[80]. The latter allows us to calculate the rate of aggregate extension L and thereby fit the time-dependent fraction of aggregates data with parameters N_o and v_N. The extraction of L is explained in more details in **Supporting Information section S.4**.
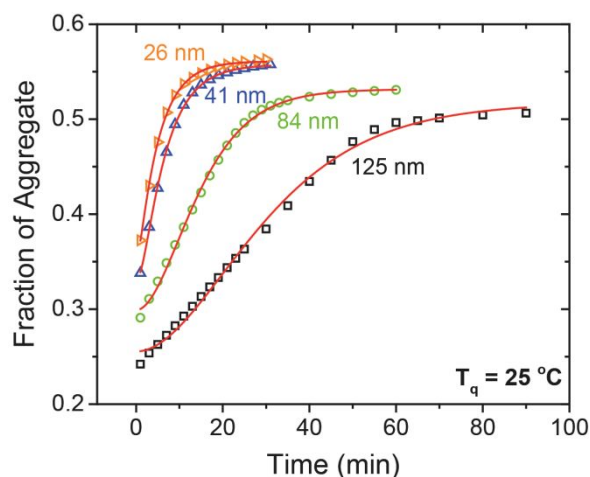
Figure 9. Plots of the fraction of aggregates of P3EHT as a function of time after being quenched from the melt to 25°C for several thicknesses. Red lines represent fits to the extended 1D Avrami model.

In **Figure 9** we have plotted the fraction of aggregates as a function of time and the fits to the data using the extended 1D Avrami model (**Equation (20)**). The results of the fit are summarized in **Table 3** and yield key insights into the crystallization dynamics of P3EHT thin films, reflecting the enhanced ease of chain reorganization via thickness confinement effects that was previously demonstrated[80]. For instance, a 125-nm thick film has a nucleation rate v_N of 0.0401 min^{-1}, which suggests that a nucleation site nucleates every 24.9 minutes on average. The total density of nucleation sites N_o for the same film is equal to 0.0445 nm^{-3} and represents the fact that there is an average of 1 nucleation site for every 22.5 cubic nanometers. As the film thickness decreases, the average nucleation rate and density of nucleation sites continually increase to 1.22 min^{-1} and 0.0669 nm^{-3} for a 26-nm thick film. Interestingly, as the film thickness decreases, the nucleation rate increases by close to two orders of magnitude whereas the density of nucleation sites increases by only ~50%. This is most likely due to the fact that the total density of nucleation sites depends on the thermodynamic properties (i.e. phase transitions and energies) of the polymer whereas the nucleation rate is greatly influenced by the reorganization kinetics of polymers chains, substrate effects, and heterogeneous versus homogeneous nucleation. This is further reflected in the rate of aggregate extension, which increases from 0.155 to 0.362 nanometers per minute as the film thickness decreases from 125 nm to 26 nm. As a whole, both the model and the insights it yields represent a useful tool for characterizing and understanding crystallization in semiconducting polymer thin films.

Table 3. Summary of modified Avrami fit to the fraction of aggregates as a function of time for P3EHT films of different thicknesses.

Thickness (nm)	A_g	A_o	L (nm min^{-1})	v_N (min^{-1})	$1/v_N$ (min)	N_o (nm^{-3})	$1/N_o$ (nm^3)
125	0.262	0.255	0.155	0.0401	24.9	0.0445	22.5
84	0.232	0.299	0.261	0.0803	12.4	0.0559	17.9
41	0.227	0.330	0.345	0.516	1.94	0.0600	16.7
26	0.206	0.355	0.362	1.22	0.820	0.0669	15.0

It is worth-mentioning here that ^{1}H TD-NMR (DF-MSE) and optical absorption can be seen as complementary techniques. Optical absorption is highly sensitive, so it can be used to probe the crystallization in thin films. However, thicker films are normally opaque to UV-VIS light, which compromise the performance of optical absorption. ^{1}H TD-NMR at low magnetic field is not as sensitivity as optical absorption, therefore to measure films with thickness from few to hundreds of nanometer is virtually impossible, because the amount of sample that would be required for a good signal-to-noise. This measurement would be more appropriated to films with thickness of micrometers. The fact that both experiments can be fitted using the same model (extended Avrami) can be taken as an evidence that even for thicker films the 1D growth is predominant and we are probing similar processes. Moreover, the comparison between ^{13}C solid-state and ^{1}H TD-NMR crystallization results presented in Fig. 5, show that ^{1}H TD-NMR is indeed probing the rate of the increase in the chain conformational order that occurs due to the crystallization, i.e., it is a molecular probe of the crystallization process. We should also mention that GIXRD results on the crystallization of P3EHT films was already reported and compared with optical absorption, showing very similar results[80]. Finally, the standard Avrami Model was previously used to study the kinetics growth of oligomers of P3HT, rendering interesting information regarding different forms of molecular arrangements[88]. However, drawing a comparison between these and the current study is not an easy task, since not only the unit cell of P3HT and P3EHT are different but, also, the type of crystal growth: the standard Avrami Model assumes a 3D crystallization growth, while the extended Avrami model considers a 1D growth.

4.   CONCLUSION

In this manuscript, we have characterized the crystal structure, molecular dynamics and crystallization kinetics of solid-state P3EHT. Using a combination of structure refined GIXD and ^{1}H-^{1}H double-quantum NMR, we confirm a tilted arrangement with difference in tilt angles of ~15º-40º degrees between pairs of adjacent polymer chains in P3EHT crystals and relatively minimal effects of the side-chain carbons on the tilt angles. ^{13}C solid-state NMR measurements reveal the presence of mobile side-chains within polymer crystals that is accompanied by an outward gradient of mobility from the thiophene main chain. Finally, we present an extended 1D Avrami model that is able to fit time-dependent solid-state NMR and optical absorption measurements to yield both the density of nucleation site and the average rate of nucleation in solid-state P3EHT. Taken as a whole, these comprehensive characterizations help us better understand local molecular dynamics and intra-crystal physical interactions in conjugated polymers that are indispensable for improving molecular design and optimizing processing conditions. The techniques described in this work also provide an aggregated set of powerful characterization tools for the future investigation of semiconducting polymers. In fact, our combined approach of GIXD and NMR offers important insights into the molecular packing and molecular mobility for polymer crystals that are complementary to state-of -the-art in the field. Recent work by Poelking[89] and Melnyk[90] et al, for instance, produced molecular packing structures and side-chain mobilities of P3HT crystals through the use of molecular dynamics (MD) simulations. On the other hand, Kayunkid et al[91] utilized high-resolution electron diffraction to produce a structural model for epitaxially-grown P3HT thin films. In conjunction with such methods, our GIXD and NMR techniques become extremely powerful tools for probing the nanoscale packing in terms of both structure and dynamics in semiconducting polymer crystals.

ASSOCIATED CONTENT

Supporting Information

AUTHOR INFORMATION

Corresponding Author
* E-mail: gcfaria@ifsc.usp.br and azevedo@ifsc.usp.br

REFERENCES

1   A. J. Heeger, *Curr. Appl. Phys.*, 2001, **1**, 247–267.
2   A. Salleo, *Mater. Today*, 2007, **10**, 38–45.
3   L. Ying, F. Huang and G. C. Bazan, *Nat. Commun.*, 2017, **8**, 1–13.
4   A. Facchetti, *Chem. Mater.*, 2011, **23**, 733–758.
5   J. Rivnay, R. M. Owens and G. G. Malliaras, *Chem. Mater.*, 2014, 26, 679–685.
6   D. T. Simon, E. O. Gabrielsson, K. Tybrandt and M. Berggren, *Chem. Rev.*, 2016, **116**, 13009–13041.
7   Y. Cao, I. D. Parker, G. Yu, C. Zhang and A. J. Heeger, *Nature*, 1999, **397**, 414–417.
8   F. Hide, M. A. Diaz-Garcia, B. J. Schwartz, M. R. Andersson, Q. Pei and A. J. Heeger, *Science (80-.).*, 1996, **273**, 1833–1835.
9   J. Bredas, D. Beljonne, V. Coropceanu and J. Cornil, *Chem. Rev.*, 2004, **104**, 4971–5003.
10   G. Li, R. Zhu and Y. Yang, *Nat. Photonics*, 2012, **6**, 153–161.
11   K. Vandewal, S. Himmelberger and A. Salleo, *Macromolecules*.
12   A. Jonsson, T. A. Sjöström, K. Tybrandt, M. Berggren and D. T. Simon, *Sci. Adv.*, 2016, **2**, 1–6.
13   A. Jonsson, S. Inal, I. Uguz, A. J. Williamson, L. Kergoat, J. Rivnay, D. Khodagholy, M. Berggren, C. Bernard, G. G. Malliaras and D. T. Simon, *Proc. Natl. Acad. Sci.*, 2016, **113**, 9440–9445.
14   H. Sirringhaus, P. Brown, R. Friend, M. Nielsen, K. Bechgaard, B. Langeveld-Voss, A. Spiering, R. Janssen, E. Meijer, P. Herwig and D. de Leeuw, *Nature*, 1999, **401**, 685–689.
15   P. M. Beaujuge and J. M. J. Fréchet, *J. Am. Chem. Soc.*, 2011, **133**, 20009–29.
16   K. Walzer, B. Maennig, M. Pfeiffer and K. Leo, *Chem. Rev.*, 2007, **107**, 1233–71.

17   M. Pfeiffer, K. Leo, X. Zhou, J. . Huang, M. Hofmann, a Werner and J. Blochwitz-Nimoth, *Org. Electron.*, 2003, **4**, 89–103.

18   C. J. Brabec, S. Gowrisanker, J. J. M. Halls, D. Laird, S. Jia and S. P. Williams, *Adv. Mater.*, 2010, **22**, 3839–56.

19   D. M. DeLongchamp, R. J. Kline, E. K. Lin, D. a. Fischer, L. J. Richter, L. a. Lucas, M. Heeney, I. McCulloch and J. E. Northrup, *Adv. Mater.*, 2007, **19**, 833–837.

20   D. Duong, M. Toney and A. Salleo, *Phys. Rev. B*, 2012, **86**, 205205.

21   K. Vakhshouri and E. D. Gomez, *Macromol. Rapid Commun.*, 2012, 2133–2137.

22   L. H. Jimison, S. Himmelberger, D. T. Duong, J. Rivnay, M. F. Toney and A. Salleo, *J. Polym. Sci. Part B Polym. Phys.*, 2013, **51**, 611–620.

23   D. H. Kim, J. T. Han, Y. D. Park, Y. Jang, J. H. Cho, M. Hwang and K. Cho, *Adv. Mater.*, 2006, **18**, 719–723.

24   W. Hourani, K. Rahimi, I. Botiz, F. P. V. Koch, G. Reiter, P. Lienerth, T. Heiser, J.-L. Budendorff and L. Simon, *Nanoscale*, 2014, **6**, 4774–4780.

25   K. Rahimi, I. Botiz, J. O. Agumba, S. Motamen, N. Stingelin and G. Reiter, *R. Soc. Chem. Adv.*, 2014, **4**, 11121–11123.

26   X. Xiao, Z. Wang, Z. Hu and T. He, *J. Phys. Chem. B*, 2010, **114**, 7452–7460.

27   K. Rahimi, I. Botiz, N. Stingelin, N. Kayunkid, M. Sommer, F. P. V. Koch, H. Nguyen, O. Coulembier, P. Dubois, M. Brinkmann and G. Reiter, *Angew. Chemie - Int. Ed.*, , DOI:10.1002/anie.201205653.

28   V. Ho, B. W. Boudouris and R. a. Segalman, *Macromolecules*, 2010, **43**, 7895–7899.

29   B. W. Boudouris, V. Ho, L. H. Jimison, M. F. Toney, A. Salleo and R. a. Segalman, *Macromolecules*, 2011, **44**, 6653–6658.

30   S. Himmelberger, D. T. Duong, J. E. Northrup, J. Rivnay, F. P. V Koch, B. S. Beckingham, N. Stingelin, R. A. Segalman, S. C. B. Mannsfeld and A. Salleo, *Adv. Funct. Mater.*, 2015, **25**, 2616–2624.

31   S. C. B. Mannsfeld, M. L. Tang and Z. Bao, *Adv. Mater.*, 2011, **23**, 127–31.

32   J. Rivnay, S. C. B. Mannsfeld, C. E. Miller, A. Salleo and M. F. Toney, *Chem. Rev.*, 2012, **112**, 5488–519.

33   B. M. Fung, A. K. Khitrin and K. Ermolaev, *J. Magn. Reson.*, 2000, **142**, 97–101.

34   A. E. Bennett, C. M. Rienstra, M. Auger, K. V. Lakshmi and R. G. Griffin, *J. Chem. Phys.*, 1995, **103**, 6951.

35   A. Bielecki, A. C. Kolbert and M. H. Levitt, *Chem. Phys. Lett.*, 1989, **155**, 341–346.

36   M. Gaborieau, R. Graf and H. W. Spiess, *Solid State Nucl. Magn. Reson.*, 2005, **28**, 160–172.

37   J. S. Frye and G. E. Maciel, *J. Magn. Reson.*, 1982, **48**, 125–131.

38   S. Hayashi and K. Hayamizu, *Bull. Chem. Soc. Jpn.*, 1991, **64**, 685–687.

39   Q. Chen, S. S. Hou and K. Schmidt-Rohr, *Solid State Nucl. Magn. Reson.*, 2004, **26**, 11–15.

40   M. Feike, D. E. Demco, R. Graf, J. Gottwald, S. Hafner and H. W. Spiess, *J. Magn. Reson. Ser. A*, 1996, **122**, 214–221.

41   R. Graf, D. E. Demco, J. Gottwald, S. Hafner and H. W. Spiess, *J. Chem. Phys.*, 1997, **106**, 885–895.

42   M. Bak, J. T. Rasmussen and N. C. Nielsen, *J. Magn. Reson.*, 2000, **147**, 296–330.

43   Z. Tosner, R. Andersen, B. Stevensson, M. Eden, N. C. Nielsen and T. Vosegaard, *J. Magn. Reson.*, 2014, **246**, 79–93.

44   F. Weigand, B. Bl??mich and H. W. Spiess, *Solid State Nucl. Magn. Reson.*, 1994, **3**, 59–66.

45   M. Goldman and L. Shen, *Phys. Rev.*, 1966, **144**, 321–331.

46   M. R. Hansen, R. Graf and H. W. Spiess, *Chem. Rev.*, 2016, **116**, 1272–1308.

47   Z. F. Chen, C. S. Wannere, C. Corminboeuf, R. Puchta and P. V Schleyer, *Chem. Rev.*, 2005, **105**, 3842–3888.

48   D. Sebastiani, *Chemphyschem*, 2006, **7**, 164–175.

49   Y. K. Lee, N. D. Kurur, M. Helmle, O. G. Johannessen, N. C. Nielsen and M. H. Levitt, *Chem. Phys. Lett.*, 1995, **242**, 304–309.

50   K. Saalwachter, F. Lange, K. Matyjaszewski, C. F. Huang and R. Graf, *J. Magn. Reson.*, 2011, **212**, 204–215.

51   M. Feike, D. E. Demco, R. Graf, J. Gottwald, S. Hafner and H. W. Spiess, *J. Magn. Reson. Ser. A*, 1996, **122**, 214–221.

52   A. Bohle, G. Brunklaus, M. R. Hansen, T. W. Schleuss, A. F. M. Kilbinger, J. Seltmann and H. W. Spiess, *Macromolecules*, 2010, **43**, 4978–4985.

53   S. P. Brown, I. Schnell, J. D. Brand, K. Mullen and H. W. Spiess, *J. Am. Chem. Soc.*, 1999, **121**, 6712–6718.

54   M. Fritzsche, A. Bohle, D. Dudenko, U. Baumeister, D. Sebastiani, G. Richardt, H. W. Spiess, M. R. Hansen and S. Hoeger, *Angew. Chemie-International Ed.*, 2011, **50**, 3030–3033.

55   J. Shu, D. Dudenko, M. Esmaeili, J. H. Park, S. R. Puniredd, J. Y. Chang, D. W. Breiby, W. Pisula and M. R. Hansen, *J. Am. Chem. Soc.*, 2013, **135**, 11075–11086.

56   D. Niedzialek, V. Lemaur, D. Dudenko, J. Shu, M. R. Hansen, J. W. Andreasen, W. Pisula, K. Muellen, J. Cornil and D. Beljonne, *Adv. Mater.*, 2013, **25**, 1939–1947.

57   R. Stalder, S. R. Puniredd, M. R. Hansen, U. Koldemir, C. Grand, W. Zajaczkowski, K. Muellen, W. Pisula and J. R. Reynolds, *Chem. Mater.*, 2016, **28**, 1286–1297.

58   H. N. Tsao, D. M. Cho, I. Park, M. R. Hansen, A. Mavrinskiy, D. Y. Yoon, R. Graf, W. Pisula, H. W. Spiess and K. Muellen, *J. Am. Chem. Soc.*, 2011, **133**, 2605–2612.

59   M. Leclerc, F. M. Diaz and G. Wegner, *Makromol. Chemie-Macromolecular Chem. Phys.*, 1989, **190**, 3105–3116.

60   T. A. Chen, X. M. Wu and R. D. Rieke, *J. Am. Chem. Soc.*, 1995, **117**, 233–244.

61   R. D. McCullough, *Adv. Mater.*, 1998, **10**, 93-+.

62   K. Schmidt-Rohr and H. W. Spiess, *Multidimensional Solid-State NMR and Polymers*, Academic Press, London, 1st edn., 1994, vol. 1.

63   D. Dudenko, A. Kiersnowski, J. Shu, W. Pisula, D. Sebastiani, H. W. Spiess and M. R. Hansen, *Angew. Chemie-International Ed.*, 2012, **51**, 11068–11072.

64   I. Schnell and H. W. Spiess, *J. Magn. Reson.*, 2001, **151**, 153–227.

65   M. R. Hansen, R. Graf, S. Sekharan and D. Sebastiani, *J. Am. Chem. Soc.*, 2009, **131**, 5251–5256.

66   M. Bak, J. T. Rasmussen and N. C. Nielsen, *J. Magn. Reson.*, 2000, **147**, 296–330.

67   I. Schnell and H. W. Spiess, *J. Magn. Reson.*, 2001, **151**, 153–227.

68   V. E. Zorin, S. P. Brown and P. Hodgkinson, *Mol. Phys.*, 2006, **104**, 293–304.

69   B. S. Beckingham, V. Ho and R. A. Segalman, *Macromolecules*, 2014, **47**, 8305–8310.

70   A. Maus, C. Hertlein and K. Saalwächter, *Macromol. Chem. Phys.*, 2006, **207**, 1150–1158.

71   M. G. Munowitz, R. G. Griffin, G. Bodenhausen and T. H. Huang, *J. Am. Chem. Soc.*, 1981, **103**, 2529–2533.

72   M. Hong, J. D. Gross and R. G. Griffin, *J. Phys. Chem. B*, 1997, **101**, 5869–5874.

73   D. Huster, L. Naji, J. Schiller and K. Arnold, *Appl. Magn. Reson.*

74   R. F. Cossiello, E. Kowalski, P. C. Rodrigues, L. Akcelrud, A. C. Bloise, E. R. Deazevedo, T. J. Bonagamba and T. D. Z. Atvars, *Macromolecules*, 2005, **38**, 925–932.

75   G. C. Farial, T. S. Plivelic, R. F. Cossiello, A. A. Souza, T. D. Z. Atvars, I. L. Torriani and E. R. Deazevedo, *J. Phys. Chem. B*, 2009, **113**, 11403–11413.

76   M. R. Hansen, R. Graf and H. W. Spiess, *Acc. Chem. Res.*, 2013, **46**, 1996–2007.

77   E. R. DeAzevedo, K. Saalwachter, O. Pascui, A. A. De Souza, T. J. Bonagamba and D. Reichert, *J. Chem. Phys.*, , DOI:10.1063/1.2831798.

78   M. F. Cobo, A. Achilles, D. Reichert, E. R. Deazevedo and K. Saalwächter, *J. Magn. Reson.*, 2012, **221**, 85–96.

79   O. F. Pascui, R. Lohwasser, M. Sommer, M. Thelakkat, T. Thurn-Albrecht and K. Saalw??chter, *Macromolecules*, 2010, **43**, 9401–9410.

80   D. T. Duong, V. Ho, Z. Shang, S. Mollinger, S. C. B. Mannsfeld, J. Dacuña, M. F. Toney, R. Segalman and A. Salleo, *Adv. Funct. Mater.*, 2014, **24**, 4515–4521.

81   A. E. Tonnelli, *NMR Spectroscopy and Polymer Microstructure: The Conformational Connection*, VCH Publishers, New York, 1989.

82   C. Hertlein, K. Saalwächter and G. Strobl, *Polymer (Guildf).*, 2006, **47**, 7216–7221.

83   J. Kang and T. Miyoshi, *Macromolecules*, 2014, **47**, 2993–3004.

84   M. Pulst, M. H. Samiullah, U. Baumeister, M. Prehm, J. Balko, T. Thurn-Albrecht, K. Busse, Y. Golitsyn, D. Reichert and J. Kressler, *Macromolecules*, 2016, **49**, 6609–6620.

85   Y. L. Hong, T. Koga and T. Miyoshi, *Macromolecules*, 2015, **48**, 3282–3293.

86   F. C. Spano, *J. Chem. Phys.*, 2005, **122**, 234701.

87   J. Clark, J.-F. Chang, F. C. Spano, R. H. Friend and C. Silva, *Appl. Phys. Lett.*, 2009, **94**, 163306.

88   F. P. V. Koch, M. Heeney and P. Smith, *J. Am. Chem. Soc.*, , DOI:10.1021/ja405792b.

89   C. Poelking and D. Andrienko, *Macromolecules*, 2013, **46**, 8941–8956.

90   A. Melnyk, M. J. N. Junk, M. D. Mcgehee, B. F. Chmelka, M. R. Hansen and D. Andrienko, *J. Phys. Chem. Lett.*, 2017, **8**, 4155–4160.

91   N. Kayunkid, S. Uttiya and M. Brinkmann, *Macromolecules*, 2010, **43**, 4961–4967.

ToC Graphic